Photocurrent Enhancement of HgTe Quantum Dot Photodiodes by Plasmonic Gold Nanorod Structures

Mengyu Chen,[†] Lei Shao,[‡,∥] Stephen V. Kershaw,[§] Hui Yu,[†] Jianfang Wang,[‡] Andrey L. Rogach,[§] and Ni Zhao[†,⊥,*]

[†]Department of Electronic Engineering, The Chinese University of Hong Kong, Shatin, New Territories, Hong Kong, [‡]Department of Physics, The Chinese University of Hong Kong, Shatin, New Territories, Hong Kong, [§]Department of Physics and Materials Science and Centre for Functional Photonics (CFP), City University of Hong Kong, Hong Kong, and [⊥]Shenzhen Research Institute, The Chinese University of Hong Kong, Hong Kong. [∥]Present address: Department of Applied Physics, Chalmers University of Technology, S-412 96 Goteborg, Sweden.

ABSTRACT The near-field effects of noble metal nanoparticles can be utilized to enhance the performance of inorganic/organic photosensing devices, such as solar cells and photodetectors. In this work, we developed a well-controlled fabrication strategy to incorporate Au nanostructures into HgTe quantum dot (QD)/ZnO heterojunction photodiode photodetectors. Through an electrostatic immobilization and dry transfer protocol, a layer of Au nanorods with uniform distribution and controllable density is embedded at different depths in the ZnO layer for systematic comparison. More than 80 and 240% increments of average short-circuit current density (J_{sc}) are observed in the devices with Au nanorods covered by ~7.5 and ~4.5 nm ZnO layers, respectively. A periodic finite-difference time-domain (FDTD) simulation model is developed to analyze the depth-dependent property and confirm the mechanism of plasmon-enhanced light absorption in the QD layer. The wavelength-dependent external quantum efficiency spectra suggest that the exciton dissociation and charge extraction efficiencies are also enhanced by the Au nanorods, likely due to local electric field effects. The photodetection performance of the photodiodes is characterized, and the results show that the plasmonic structure improves the overall infrared detectivity of the HgTe QD photodetectors without affecting their temporal response. Our fabrication strategy and theoretical and experimental findings provide useful insight into the applications of metal nanostructures to enhance the performance of organic/inorganic hybrid optoelectronic devices.

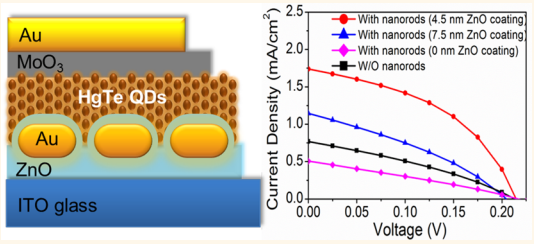

KEYWORDS: quantum dot · surface plasmon · heterojunction · exciton

Use of the light-trapping property of metallic nanostructures in photosensing devices, such as solar cells and photodetectors, has been extensively studied in the past decades.[1−3] Among various metallic nanostructures colloidal noble metal nanoparticles (NPs) are particularly promising due to their simple synthesis, solution processability and tunable shapes for diverse wavelengths applications.[3−6] When embedded in a material, metal NPs trigger the redistribution of the electromagnetic-field by coupling with the incident light at the localized surface plasmon resonance (LSPR) frequency; the light absorption of the surrounding material can be improved *via* both the near-field electromagnetic-field enhancement and the increase of the optical-path length caused by the light-scattering of the metal NPs.[1,7,14] Such amplification of light absorption (within the active component of the devices) has been applied to inorganic-based photodetectors and solar cells,[8−10] organic solar cells,[11−18] dye-sensitized solar cells[19−22] and perovskite-based solar cells.[23] Early studies showed that directly blending metal NPs into the photoactive layer of a device leads to little or no photocurrent improvement even though the plasmon-enhanced optical absorption is significant. This is mainly due to exciton quenching and trap-assisted charge recombination at the surface of the metal NPs.[12,18,24] Recent research demonstrated alternative approaches such as doping Au-TiO_2 core−shell nanoparticles into the porous TiO_2 layer of dye-sensitized solar cells[20,22] and embedding self-assembled

* Address correspondence to nzhao@ee.cuhk.edu.hk.

Received for review May 8, 2014 and accepted July 14, 2014.

Published online July 14, 2014
10.1021/nn502510u

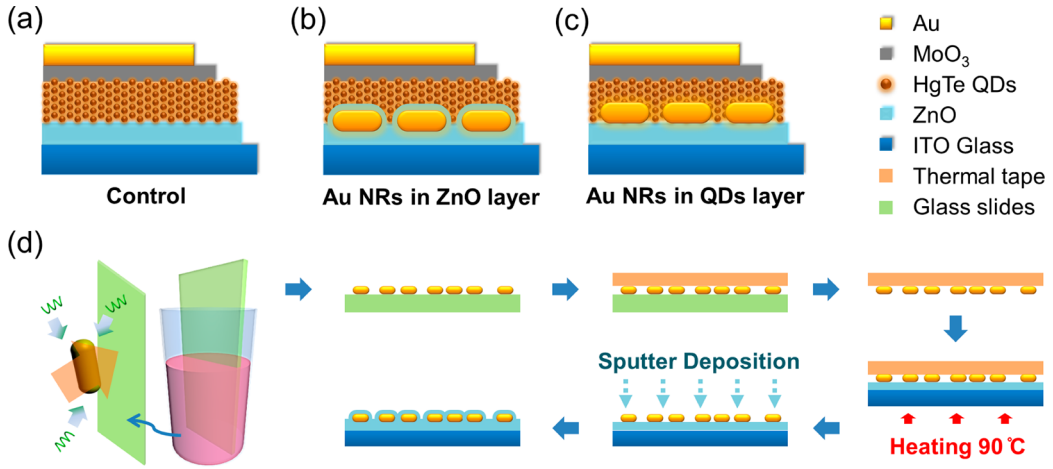

Figure 1. (a) The control (or reference) device structure for HgTe QDs/ZnO heterojunction photodiodes (without Au nanorods). (b) HgTe QDs/ZnO heterojunction photodiode with Au nanorods embedded within ZnO layer (Au nanorods with ZnO coating). (c) HgTe QDs/ZnO heterojunction photodiode with Au nanorods embedded within the QD layer (nanorods with no ZnO coating). (d) The fabrication methodology of the ZnO substrates with embedded Au nanorods as for structure (b), including the electrostatic immobilization of Au nanorods and the thermal release tape dry-transfer process.

Au nanopyramid arrays into the poly(3,4-ethylenedioxythiophene)-poly(styrenesulfonate) (PEDOT:PSS) buffer layer of organic solar cells.[16] These studies achieved up to 50% increment of the short-circuit current density (J_{sc}) thanks to the surface passivation and good dispersion of the Au NPs in the buffer layers. So far most work relied on either coblending or template-growth methods to incorporate metal NPs into the device structures. To take the full advantage of metal NP nanostructures in photosensing devices, it is crucial to precisely tune the position of the NPs relative to the photoactive layer as well as to understand how the presence of metal nanostructures affects the light absorption and charge generation/transport processes in a device.

In this work, we demonstrate a well-controlled fabrication strategy to embed metal NP-based plasmonic structures in quantum dot (QD)/ZnO heterojunction photodiodes for photodetection application. By using electrostatic immobilization and a dry transfer method, a layer of Au nanorods with uniform distribution and controllable density is embedded at different depths in the sputtered ZnO electron-transporting layer. HgTe QDs are chosen as the model photoactive material because they have shown promising performance as photodetectors with wide spectral range (from near-infrared (NIR) to mid-infrared (MIR)[25]) and fast temporal response.[26] Using the embedded Au nanorod structures we have achieved a remarkable enhancement of up to 240% for the photocurrent of the devices. The measured wavelength-dependent extinction spectra confirm the LSPR enhanced absorption and are well fitted with a finite-difference time-domain (FDTD) simulation with a single particle model. Periodic FDTD simulation is also performed to analyze the depth-dependent property of the plasmonic structure. The wavelength-dependent external quantum efficiency spectra suggest that the plasmon-enhanced light absorption alone cannot account for the remarkable enhancement of the photocurrent. Other factors, such as geometric electric field enhancement (GEFE),[27] local electric field-assisted exciton dissociation,[14,20−23] and localized plasmon heating[22,28−30] may also play an important role in assisting the charge generation and extraction in the photodiodes.

RESULTS AND DISCUSSION

Device Structures and Fabrication Strategy. Figure 1(a−c) shows the schematic configurations of the device structures used in this study. The control device consisted of a HgTe QD/ZnO heterojunction sandwiched between a Au/MoO_3 top contact and ITO-coated glass. For devices with plasmonic Au structures, the Au nanorods were embedded at different depths of the ZnO layer or at the QD/ZnO interface for systematic comparison. The energy diagram of the control device is shown in Figure S1 in the Supporting Information. Under illumination from the ITO glass side, the photoexcited electron−hole pairs are generated in the QD layer and are dissociated either in the QD layer or at the QD/metal oxide interfaces. The electrons and holes are then collected by the ITO and Au electrodes, respectively.

The HgTe QDs used in this study were synthesized in aqueous solutions *via* a room temperature reaction between $Hg(ClO_4)_2$ and H_2Te gas in the presence of 1-thioglycerol (TG).[31,32] The average diameter of the HgTe QDs is about 3.1 nm, corresponding to a photoluminescence (PL) wavelength at around 1300 nm.[32,33] A spray-coating process was applied to deposit the HgTe QD layers. The detailed preparation method for the spray-coating deposition of the aqueous HgTe QD solution can be found in our previous work.[26] The QD concentration and number of spray passes were kept the same for all the devices. Before QD deposition the

substrates were treated with oxygen plasma for 100 s to obtain a hydrophilic surface. The thickness of the HgTe QD layers was about 160 nm. After the fabrication of QD layer, a 10 nm MoO_3 buffer layer and a 60 nm Au electrode were deposited sequentially by thermal evaporation.

RF magnetron sputtering was used to deposit the ZnO layer. The thickness of the ZnO layer was controlled by the sputtering time. Figure 1(d) shows the fabrication method used to embed the Au nanorod structures in the ZnO layer. First, the Au nanorods were prepared by a seed-mediated growth procedure and stabilized with cetyltrimethylammonium bromide (CTAB) in aqueous solution.[6,34] Second, the glass slides, which were pretreated in ethanol and cleaned by oxygen plasma, were immersed into the as-grown Au nanorod solution and left undisturbed for 4 h. Since the glass surface is covered with hydroxyl groups and therefore negatively charged, the positively charged CTAB-stabilized Au nanorods tend to attach to the glass surface *via* electrostatic attraction. The density of the Au nanorods can be controlled by the concentration of CTAB. As described in previous work,[34] this electrostatic immobilization technique can realize high-density, well-dispersed deposition of various colloidal Au NPs, including nanospheres, nanorods and nanobipyramids. To transfer the nanorods onto the ZnO layer, we used a thermal-release tape as a temporary holder, an approach that is widely used for graphene transfer.[35,36] As shown in the right part of Figure 1(d), the thermal-release tape was first brought into contact with the Au nanorod monolayer and then slowly peeled off from the glass substrates. The tape with the Au nanorods was then attached to the ZnO/ITO glass substrate. At a temperature of 90 °C, the thermal-release tape will lose its attachment to the Au nanorods, leaving the majority of them on the ZnO surface. To form the embedded structure shown in Figure 1(b), a second layer of ZnO is sputtered onto the surface of Au nanorods. Note that the total thickness of the ZnO layer is kept at 30 nm for all the device structures studied herein. Accordingly, for the embedded structure the thicknesses of the first and second sputtered ZnO layers combined was 30 nm in total.

Figure 2(a) shows an SEM image that reveals the typical distribution of Au nanorods electrostatically immobilized on a glass slide. The nanorods were uniformly distributed and well separated with a density of 35–40 rods per μm^2. The inset of Figure 2(a) shows the TEM image of the Au nanorods, which are 40–50 nm wide and 90–110 nm long, leading to an LSPR wavelength at around 690 nm in water (dominated by the longitudinal resonance)[6,34] and at around 900 nm in the HgTe QD/ZnO devices (confirmed by the FDTD simulation and spectral extinction measurements discussed in later sections). Figure 2(b) reveals the typical

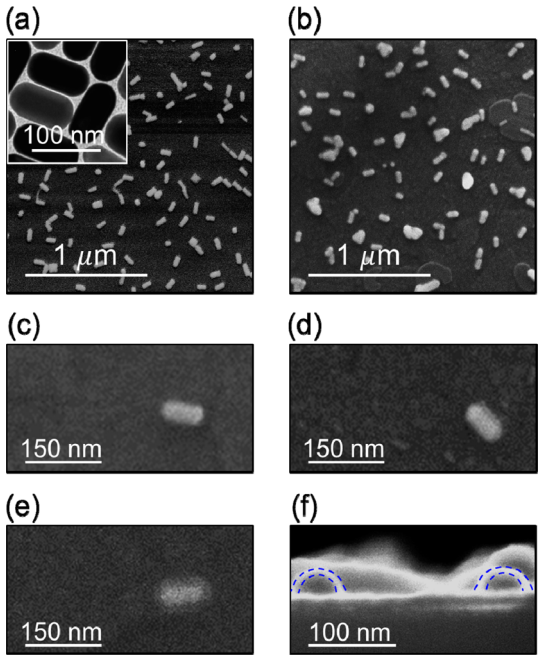

Figure 2. (a) SEM image of the distribution of Au nanorods on glass slides after electrostatic immobilization (before thermal tape transfer). Inset: TEM Image of the Au nanorods used in this work. (b) SEM image of the distribution of Au nanorods after thermal tape dry transfer to the sputtered ZnO layer. (c–e) SEM images of single Au nanorods without ZnO coating, with 3 min sputtering ZnO coating, and with 5 min sputtering ZnO coating, respectively. (f) SEM image of the cross-section of Au nanorods with 5 min sputtering ZnO coating. The core (Au nanorod) and the shell (ZnO coating) structures are highlighted by blue dashed lines.

distribution of Au nanorods after the thermal tape dry transfer. The nanorod distribution was relatively uniform with slightly increased rod aggregation, while their density dropped to 25–30 rods per μm^2. Therefore, about 75% of the Au nanorods were transferred. Next, we examined the morphology of individual Au nanorods with ZnO coating. The SEM top views of Au nanorods without ZnO and with 3 and 5 min sputtered ZnO coatings are shown in Figure 2(c–e), respectively. The ZnO conformally coats over the Au nanorods and the coating thickness increases with the sputtering time. The SEM image of the cross-section of Au nanorods with 5 min sputtered ZnO coating is shown in Figure 2(f). The core (Au nanorods) and shell (ZnO coating) structures are highlighted by blue dashed lines. The average thickness of the ZnO coating over the top of the nanorods is around 7.5 nm. Considering that the thickness of ZnO is linearly proportional to the sputtering time, the average thickness of the 3 min sputtered ZnO coating should be around 4.5 nm.

Performance Comparison. The current–voltage characteristics of the photodiodes with different device structures are compared in Figure 3. For each structure more than 20 devices were fabricated, and the comparison between the structures was summarized from different device batches. Although the device performance

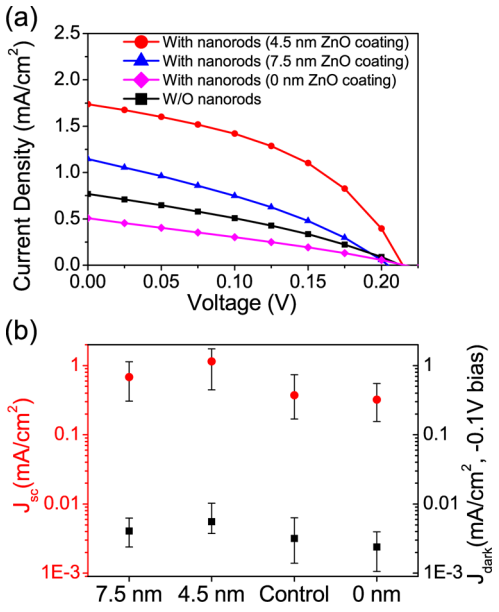

Figure 3. Comparison of the device performance of different structures. (a) Representative *J*−*V* curves of control devices without Au nanorods, devices with 4.5 and 7.5 nm ZnO coated Au nanorods (as in Figure 1(b)), and devices with Au nanorods in direct contact with the QD layer (0 nm coating, as in Figure 1(c)). (b) Statistical comparison (over 20 devices for each case) of the short circuit current densities and the dark current densities (−0.1 V bias) in the different cases described in (a). The photocurrents of all the devices were measured under AM1.5 simulated sunlight with a 420 nm long-pass UV edge filter. The UV part of the spectrum was blocked because it can cause variations in the conductivity of the ZnO.[37]

varies with the QD quality in different batches, the relative trends between each structure are highly reproducible. As shown in Figure 3(b), the average J_{sc} of the control devices (with no Au nanorods) is 0.37 mA/cm^2, whereas the devices embedded with Au nanorods in the ZnO layer can reach average J_{sc} values of 0.68 mA/cm^2 for 7.5 nm ZnO and 1.27 mA/cm^2 for 4.5 nm ZnO layer thicknesses, which correspond to a remarkable enhancement of 83 and 243%, respectively. For the devices with Au nanorods positioned at the QD/ZnO interface (Figure 1(c)), the average J_{sc} is 0.35 mA/cm^2, a little lower than that of the control devices. This observation is consistent with previous studies[12,18,24] and is likely due to exciton quenching and trap-assisted charge recombination at the Au nanorod surface. This argument is further supported with the transient photovoltage measurement of the photodiodes (Figure S2 in the Supporting Information), where the QD/Au nanorod/ZnO structure exhibits much faster transient photovoltage decay than the other device structures. The time-resolved photoluminescence measurement of the HgTe QD/ZnO films (Figure S3 in the Supporting Information) also suggests strong exciton quenching at the Au nanorod surface. It is also worth noting that there may exist a certain degree of interdiffusion between Au and Hg atoms,[38] which could introduce a large number of interface traps as well as suppressing the LSPR property of the Au nanorods.

The dark current density (at −0.1 V bias), which determines the noise level in the photodetectors, is also measured for different devices as shown in Figure 3(b). It exhibits a similar trend as the light current density but with much smaller variation in the magnitude. This result suggests that the Au nanorod structure can improve the photocurrent without sacrificing too much in the noise level; therefore enhancement in the overall detectivity of the HgTe QD photodetectors can be achieved (discussed in a later section).

Enhancement in Optical Absorption. To investigate the origin of the photocurrent enhancement in the embedded Au nanorod devices, the optical absorption of the HgTe QD/ZnO films with and without the embedded Au nanorods was first measured. The thin film samples were fabricated on ITO glass substrates following the same conditions as the photodiode devices. Figure 4(a) shows the measured extinction spectra of these films. A significant enhancement of the extinction is observed in the 500−1300 nm range for the QD/ZnO films with embedded Au nanorods. Beyond 1300 nm there is a plateau in all the spectra, which may originate from the light scattering due to the rough surface of the spray-deposited HgTe QDs. To facilitate comparison, the extinction increments of the HgTe QD/ZnO films with embedded Au nanorods are plotted in Figure 4(b). More than 30% enhancement at the peak position around 900 nm is observed for both samples with 4.5 and 7.5 nm ZnO coated Au nanorods. The FDTD simulated extinction cross-section spectra of a single Au nanorod, both in the longitudinal and transverse directions, are also normalized and given in Figure 4(b) for comparison. The measured extinction increment peaks match well with the longitudinal surface plasmon resonance peak of the Au nanorod, which shows that the improvement in the optical absorption of our devices is closely related to the LSPR of Au nanorods. There is no obvious peak corresponding to the extinction enhancement from the transverse LSPR of the Au nanorods, which is possibly smeared out by the dominant longitudinal resonance and the strong extinction of the QD film in the 400−500 nm wavelength range.

Besides the widely used single particle model,[6,22] which can only simulate the extinction cross-section spectrum around a plasmonic particle, a periodic model of Au nanorods is also developed in our FDTD simulation. In this model the Au nanorods are assumed to be periodically patterned without a strong coupling effect, and the close-packed HgTe QD layer is considered as a uniform effective medium.[39] Although this model idealizes the distribution of Au nanorods to be periodic, which is not the case in the real devices, it can still reflect the absorption profile of QDs in the vicinity of Au nanorods.

Figure 5(a) shows the simulated 2D light absorption distribution at the dominant longitudinal LSPR peak

wavelength for the HgTe QD/ZnO films without and with embedded Au nanorods. The thicknesses of the ZnO top coatings are set to 15, 7.5 and 2.5 nm, respectively. The absorption distribution at a given position can be calculated as

$$P_{abs}(x,y,z,\omega) = \nabla\cdot\left(\frac{1}{2}\text{real}(\vec{E}(x,y,z,\omega)\times\vec{H}^{*}(x,y,z,\omega))\right) = \frac{1}{2}\omega E(x,y,z,\omega)E(x,y,z,\omega)^{*}\text{Im}(\varepsilon_{material}(\omega)) \quad (1)$$

where $\vec{E}$ and $\vec{H}$ are the electric-field and magnetic-field of the incident light, and $\varepsilon_{material}$ is the complex relative permittivity of the material.[39] As shown in Figure 5(a), the incident light is mainly absorbed by two components, the HgTe QD layer and the Au nanorods. The light absorption in the QD layer is affected by the enhancement of the local electromagnetic field, which is arises from the resonant collective electron oscillation within the Au nanorods. The absorption in the QD layer therefore varied with the thickness of the ZnO top coating: the thinner the coating, the stronger the near-field effect and thus the absorption intensity. On the other hand, the Au nanorods themselves exhibit strong absorption. Figure 5(b) shows the calculated total absorption spectra considering both absorbing components. In this case the peak intensity is not sensitive to the position of the embedded Au nanorods in the ZnO layer due to the strong absorption from the metal itself. However, if we only calculate the absorption in the HgTe QD layer, *i.e.*, the effective component for photocurrent generation, the depth-dependent absorption enhancement by the Au nanorods is then more obvious, as shown in Figure 5(c). These simulation results explain partially why the 4.5 and 7.5 nm ZnO coated Au nanorod structures resulted in different

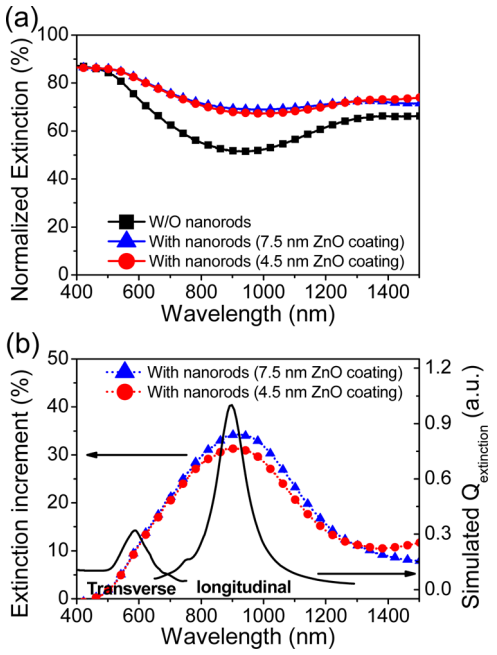

Figure 4. (a) Measured extinction spectra of HgTe QD/ZnO films without Au nanorods and with 7.5 and 4.5 nm ZnO coated Au nanorods, respectively. (b) Extinction increments of HgTe QD/ZnO films with ZnO coated Au nanorods normalized by the extinction spectrum of the control sample. The normalized FDTD simulated extinction cross-section spectra with the longitudinal and transverse LSPRs of Au nanorods coated with 7.5 nm ZnO in HgTe QD layer is also shown.

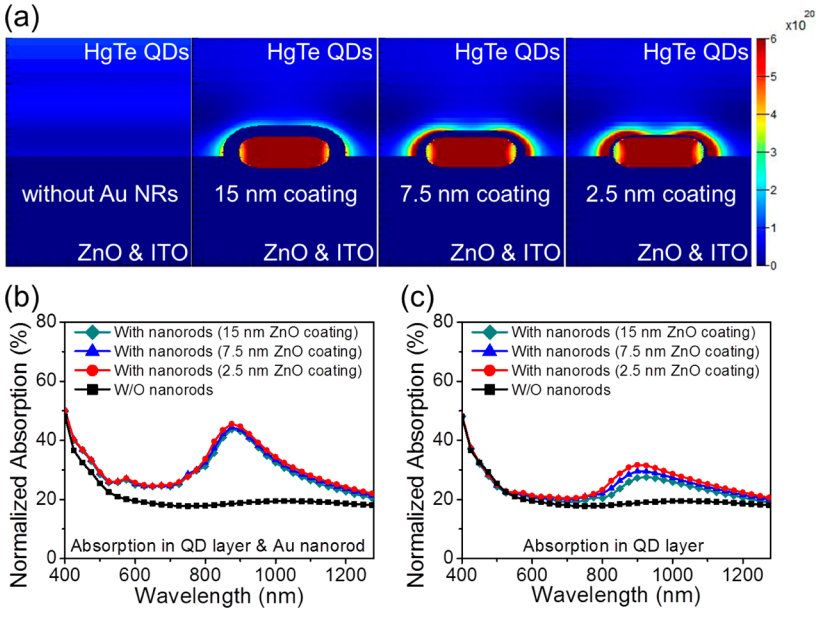

Figure 5. (a) FDTD simulated 2D light absorption distributions (cross sections) of the HgTe QD/ZnO films with and without Au nanorods at the LSPR peak wavelength. The thicknesses of the ZnO coatings are set to 15, 7.5 and 2.5 nm, respectively. The polarization of the incident wave is along the long-axis of the Au nanorods. (b) Simulated total absorption spectra of the four cases shown in (a) by accounting for the absorption in the whole film. (c) Simulated absorption spectra of the four cases shown in (a) by only accounting for the absorption in the QD films.

photocurrents in the HgTe QD/ZnO devices although they seem to provide the same amount of total enhancement in the extinction spectra in Figure 4(a).

Enhancement in External Quantum Efficiency. Although we have demonstrated both theoretically and experimentally the plasmon enhanced absorption in the QD layer, the up to 35% increment in the optical absorption alone cannot explain the respective 80 and 240% increase of the photocurrent in the devices with ~7.5 and ~4.5 nm ZnO covered Au nanorods. To further understand the underlying mechanisms for the photocurrent enhancement, we measured the external quantum efficiency (EQE) spectra of the photodiodes with different structures. As shown in Figure 6(a), the EQE enhancement in the 4.5 and 7.5 nm nanorod-embedded devices is broadly distributed over the whole measurement range and peaks at 1200−1300 nm, 300 nm red-shifted as compared to the extinction spectra. This result suggests that the presence of the Au nanostructures not only increases the optical absorption but also modifies the local electronic environment to facilitate exciton dissociation and charge extraction within the photodiodes, a phenomenon that has also been observed in other nanostructured semiconductor devices.[14,18,20−23]

The EQE enhancement likely results from the interplay of several factors besides the absorption improvement: First, the surface plasmon can strongly modify the exciton dynamics through plasmon-exciton coupling, which has been shown to facilitate the exciton dissociation process.[14,20,23] Second, the presence of Au nanorods produces ~40 nm protrusions widely distributed in the QD layer. This induces a geometric electric field enhancement (GEFE) effect around the nanoprotrusions, thus increasing the driving force for charge separation[40,41] and charge extraction.[27] It is worth mentioning that the average dark current of nanorod-embedded devices is slightly higher than the control devices (Figure 3(b)), which may be another indication of the GEFE effect. Third, the energy absorbed within the Au nanorods and consumed by the electron resonance may partially thermally dissipate into the surrounding environment and increase the local temperature,[22,28−30] which could also change the dynamic properties of excitons and charges. We note that the above mechanisms would all increase the EQE in a broad photoexcitation wavelength range. The fact that the EQE enhancement peaks at 1200 nm, just above the bandgap wavelength (1300 nm) of the HgTe QDs, suggests that the energy requires to dissociate excitons increases with the excitation wavelength.[40,41] Hot excitons or hot charge transfer states, which are generated by the excess photon energy above the bandgap, were recently observed in various nanostructured semiconductors such as QD/metal oxide, QD/polymer and polymer/fullerene blends.[42−46] Therefore, the hot charge transfer process may dominate the photon-to-electron conversion efficiency at

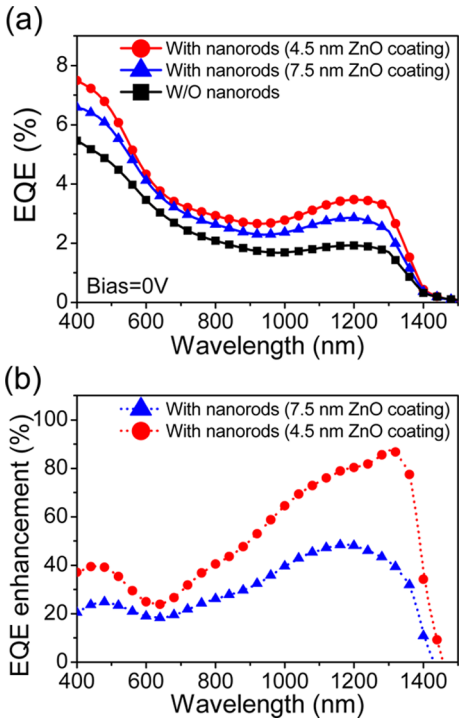

Figure 6. (a) Measured external quantum efficiency (EQE) spectra of the representative devices shown in Figure 3(a), including the control device without the nanorods and the devices with ZnO coated (7.5 and 4.5 nm) Au nanorods. (b) EQE increments of the devices with ZnO coated Au nanorods normalized by the EQE spectrum of the control device. All devices were measured under 0 V bias.

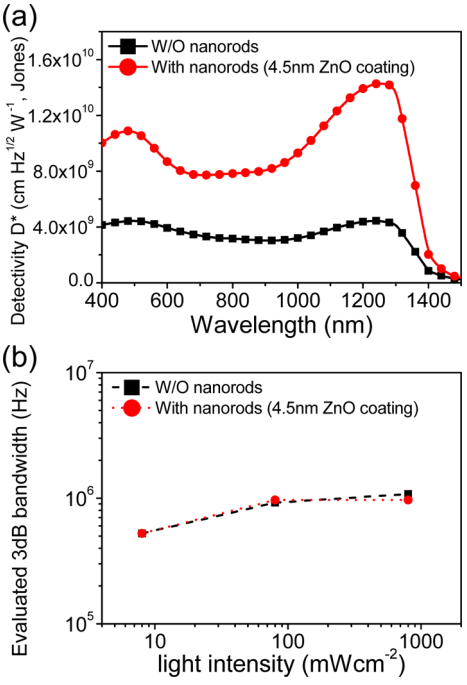

Figure 7. (a) Detectivity spectra evaluated from the EQE spectra and the dark current noise levels of the photodiodes with and without the embedded nanorod structures. (b) The evaluated 3 dB bandwidth extracted from the light intensity-dependent transient photocurrent decays of the same devices in (a). All devices were measured under 0 V bias.

short-wavelength excitations, while the aforementioned near-field effects could play a more important role in exciton dissociation for longer wavelength excitations. To further understand and utilize the enhancement mechanisms introduced by the Au plasmonic nanostructures, a systematic study combining time-resolved spectroscopic measurements and theoretical calculations of exciton−plasmon coupling is required.

In the end, we evaluate the wavelength-dependent detectivity of the photodiodes based on the EQE spectra and the noise values extracted from the dark current of the devices. (The detailed extraction method is described in ref 47.). Figure 7(a) compares the devices without the Au nanorods and with the 4.5 nm ZnO coated Au nanorods. It can be seen that the detectivity is enhanced across the whole spectrum and in particular, more than 200% increment of the detectivity is achieved in the 1000 to 1350 nm wavelength range by the embedded Au nanorod structure. The light intensity-dependent 3 dB bandwidth of the devices is shown in Figure 7(b). The bandwidth values are evaluated from the time constants τ of the transient photocurrent decays.[47] The response speed of the devices with and without the embedded Au nanorod structure remains similar under different light illumination levels, which suggests that the charge recombination process at zero bias is little affected by the embedded Au nanostructures.

CONCLUSION

In summary, we have developed a well-controlled fabrication strategy for colloidal metal NP plasmonic structures and applied it to HgTe QD/ZnO heterojunction photodiodes. By placing the Au nanorods at different layer positions within the photodiodes, we investigated several enhancement mechanisms at play due to the metal nanostructures. More than 80 and 240% increments of the average J_{sc} values were observed in the devices with Au nanorods embedded below 7.5 and 4.5 nm ZnO layers, respectively. Such depth-dependent enhancement suggests strong near-field effects induced by the Au nanostructures. The extinction spectra of the nanorod-embedded QD/ZnO films confirm the LSPR enhanced optical absorption and are well fitted with FDTD simulations. The wavelength-dependent EQE enhancement suggests that the Au nanorod structures also facilitated exciton dissociation and charge extraction in the devices. Overall, the embedded plasmonic structure improves the infrared detectivity of the HgTe QD photodiode photodetectors without affecting their temporal response. Our fabrication strategy and theoretical and experimental findings shed new light on the design and applications of metal nanostructures for the performance enhancement of organic/inorganic optoelectronic devices.

METHODS

Device Fabrication. The prepatterned ITO glass substrates were cleaned by deionized water, acetone, isopropanol and oxygen plasma treatments before the ZnO layer deposition. The ZnO layer was fabricated with an Anatech Magnetron Sputtering Machine with 80 W RF power, and the deposition rate was about 3 nm per minute. The ZnO coated substrates were treated with oxygen plasma for 100 s just before the spray-coating of the QDs.

The HgTe QDs were precipitated from as-grown solution by adding methanol followed by centrifugation and then redissolved in deionized water before the spray coating process. For the layer-by-layer spray-coating deposition, the substrate temperature was kept around 45 °C and a nitrogen gas flow was introduced above the substrate surface to control the drying process. The concentration of the aqueous HgTe QD solution for spray-coating was about 40−50 mg/mL. The nozzle of the spray airbrush was 300 nm with a distance of 11 cm to the substrate placed on a hot plate. The pressure of the spraying and blowing gas was set to 0.5 bar. After about 50 passes, the thickness of the QD films could reach 150−200 nm.

The electrostatic immobilization and dry transfer process of Au nanorods included the following steps: First, the CTAB concentration in the as-grown Au nanorod solution was greatly reduced by two cycles of precipitation and redispersion of the nanorods in deionized water. Then, glass slides, which were treated by ultrasonication in ethanol for at least 30 min and further cleaned in an oxygen plasma, were immersed into the washed Au nanorod solution and left undisturbed for 4 h. The deposition density of the Au nanorods was controlled by the CTAB concentration. For the thermal release tape dry transfer process, the tapes were directly purchased from Graphene Square Inc. The transfer process is shown in Figure 1(d).

SEM imaging was carried out on an FEI Quanta 400 FEG microscope. TEM imaging was performed on an FEI Tecnai Spirit microscope operated at 120 kV.

Characterization. The current−voltage characteristics were measured in a glovebox with a Keithley 2612 Source Meter both in the dark and under illumination by a Newport 94011A-ES Sol series Solar Simulator (AM1.5) with a 420 nm long-pass UV edge filter.

The extinction spectra of the HgTe QD/ZnO films with and without the Au nanorods were measured with a Hitachi U-3501 UV−vis−NIR spectrophotometer, where the transmission through the thin film samples are recorded and used to estimate the extinction coefficient.

External quantum efficiencies were measured with a Keithley 2400 Source Meter under monochromatic illumination generated by passing the light beam from a 250W quartz tungsten halogen (QTH) lamp into a Newport 74125 Oriel Cornerstone 260 1/4 m monochromator. The optical power density was measured to be about 1 mW/cm^2 at λ = 800 nm. A silicon photodetector and a germanium photodetector were used to calibrate the optical power density of the spectrally resolved output from 400 to 1100 nm and 800 to 1500 nm, respectively.

Transient Photovoltage Measurement. A Newport LQD635−03C laser diode, with square-wave modulation, was used to illuminate the devices. The anode and cathode of the device were connected across a 1 MΩ load resistor and connected to a Tektronix TDS 3014C Oscilloscope allowing the modulated changes in the photovoltage under open circuit condition to be recorded.

Transient Photocurrent Measurement. A Newport LQD635−03C laser diode, with square-wave modulation at different frequencies, was used to illuminate the devices. The resulting

photocurrent was amplified by a Femto DHPCA-100 High Speed Current Amplifier and measured with a Tektronix TDS 3014C Oscilloscope. The photocurrent decays and the related time constants were measured with a pulse repetition frequency of 51 Hz.

Time-Resolved Photoluminescence Measurement. Photoluminescence (PL) spectra were measured on an Edinburgh Instrument FLS920P fluorescence spectrometer, with a xenon lamp as the excitation source for the steady-state spectra and a picosecond pulsed diode laser (EPL-670 nm, pulse width: 49 ps) for lifetime (time-correlated single-photon counting, TCSPC) measurements. The detector was a Hamamatsu R5509−73 InP/InGaAs cooled NIR photomultiplier tube.

FDTD Simulation. The simulation models were designed using the commercial software Lumerical FDTD, with the material parameters of HgTe QD films from previously reported ellipsometry measurements.[48] The dimensions of the Au nanorods, the relative positions and thicknesses of ITO, ZnO and HgTe QD layer were matched carefully to the experimentally determined parameters of the fabricated devices. For the single particle model, a total-field scattered-field source (TFSF) was used to surround one Au nanorod and calculate the absorption and scattering cross sections (the extinction cross section being the sum of them). For the periodic model, we assumed that the device extends infinitely in the $x-y$ plane. The dimensions of one unit cell in the $x-y$ plane was set to be 182 nm $\times$ 182 nm with the "periodic" boundary conditions mimicking the typical distribution density of Au nanorods in our devices, 30 particles per μm^2.

Conflict of Interest: The authors declare no competing financial interest.

Acknowledgment. We gratefully acknowledge fundings from the National Science Foundation of China (Grant No. 61205036), the Shun Hing Institute of Advanced Engineering (Grant No. 8115041) and the Direct Grant from Chinese University of Hong Kong (Grant No. 4055012). This work was also supported by an Applied Research Grant of City University of Hong Kong (9667067), and by grants from the Research Grants Council of the Hong Kong S.A.R., China (Project CityU 102412 and CUHK401511).

Supporting Information Available: The energy diagram of HgTe QD/ZnO heterojunction corresponding to the photodiode structures is shown in Figure S1; The transient photovoltage measurement results of the control device, the devices with Au nanorods in the ZnO layer, and the device with Au nanorods at the QD/ZnO interface are shown in Figure S2; the normalized time-resolved photoluminescence transients of HgTe QD/ZnO films with and without the Au nanorods are shown in Figure S3. This material is available free of charge *via* the Internet at http://pubs.acs.org.

REFERENCES AND NOTES

1. Konstantatos, G.; Sargent, E. H. Nanostructured Materials for Photon Detection. *Nat. Nanotechnol.* **2010**, *5*, 391–400.
2. Schuller, J. A.; Barnard, E. S.; Cai, W.; Jun, Y. C.; White, J. S.; Brongersma, M. L. Plasmonics for Extreme Light Concentration and Manipulation. *Nat. Mater.* **2010**, *9*, 193–204.
3. Maier, S. A. *Plasmonics: Fundamentals and Applications*; Springer Science+Business Media LLC: New York, 2007; Chapter 1, Vol. 2, p 5.
4. Mock, J. J.; Barbic, M.; Smith, D. R.; Schultz, D. A.; Schultz, S. Shape Effects in Plasmon Resonance of Individual Colloidal Silver Nanoparticles. *J. Chem. Phys.* **2002**, *116*, 6755–6759.
5. Kuwata, H.; Tamaru, H.; Esumi, K.; Miyano, K. Resonant Light Scattering from Metal Nanoparticles: Practical Analysis beyond Rayleigh Approximation. *Appl. Phys. Lett.* **2003**, *83*, 4625–4627.
6. Ni, W.; Kou, X.; Yang, Z.; Wang, J. Tailoring Longitudinal Surface Plasmon Wavelengths, Scattering and Absorption Cross Sections of Gold Nanorods. *ACS Nano* **2008**, *2*, 677–686.
7. Catchpole, K. R.; Polman, A. Plasmonic Solar Cells. *Opt. Express* **2008**, *16*, 21793–21800.
8. Derkacs, D.; Lim, S. H.; Matheu, P.; Mar, W.; Yu, E. T. Improved Performance of Amorphous Silicon Solar Cells *via* Scattering from Surface Plasmon Polaritons in Nearby Metallic Nanoparticles. *Appl. Phys. Lett.* **2006**, *89*, 093103.
9. Nakayam, K.; Tanabe, K.; Atwater, H. A. Plasmonic Nanoparticle Enhanced Light Absorption in GaAs Solar Cells. *Appl. Phys. Lett.* **2008**, *93*, 121904.
10. Ouyang, Z.; Pillai, S.; Beck, F.; Kunz, O.; Varlamov, S.; Catchpola, K. R.; Campbell, P.; Green, M. A. Effective Light Trapping in Polycrystalline Silicon Thin-Film Solar Cells by Means of Rear Localized Surface Plasmons. *Appl. Phys. Lett.* **2010**, *96*, 261109.
11. Chen, F.-C.; Wu, J.-L.; Lee, C.-L.; Hong, Y.; Kuo, C.-H.; Huang, M. H. Plasmonic-enhanced Polymer Photovoltaic Devices Incorporating Solution-Processable Metal Nanoparticles. *Appl. Phys. Lett.* **2009**, *95*, 013305.
12. Topp, K.; Borchert, H.; Johnen, F.; Tunc, A. V.; Knipper, M.; von Hauff, E.; Parisi, J.; Al-Shamery, K. Impact of the Incorporation of Au Nanoparticles into Polymer/Fullerene Solar Cells. *J. Phys. Chem. A* **2010**, *114*, 3981–3989.
13. Yang, J.; You, J.; Chen, C.-C.; Hsu, W.-C.; Tan, H.; Zhang, X. W.; Hong, Z.; Yang, Y. Plasmonic Polymer Tandem Solar Cell. *ACS Nano* **2011**, *5*, 6210–6217.
14. Wu, J.-L.; Chen, F.-C.; Hsiao, Y.-S.; Chien, F.-C.; Chen, P.; Kuo, C.-H.; Huang, M. H.; Hsu, C.-S. Surface Plasmonic Effects of Metallic Nanoparticles on the Performance of Polymer Bulk Heterojunction Solar Cells. *ACS Nano* **2011**, *2*, 959–967.
15. Xie, F.-X.; Choy, W. C. H.; Wang, C. C. D.; Sha, W. E. I.; Fung, D. D. S. Improving the Efficiency of Polymer Solar Cells by Incorporating Gold Nanoparticles into All Polymer Layers. *Appl. Phys. Lett.* **2011**, *99*, 153304.
16. Kirkeminde, A.; Retsch, M.; Wang, Q.; Xu, G.; Hui, R.; Wu, J.; Ren, S. Surface-Passivated Plasmonic Nano-pyramids for Bulk Heterojunction Solar Cell Photocurrent Enhancement. *Nanoscale* **2012**, *4*, 4421–4425.
17. Li, X.; Choy, W. C. H.; Lu, H.; Sha, W. E. I.; Ho, A. H. P. Efficiency Enhancement of Organic Solar Cells by Using Shape-Dependent Broadband Plasmonic Absorption in Metallic Nanoparticles. *Adv. Funct. Mater.* **2013**, *23*, 2728–2735.
18. Huang, Y.-F.; Zhang, Z.-L.; Kang, K.-B.; Zhao, M.; Wen, T.; Liu, Y.-X.; Zhai, X.-P.; Lv, S.-K.; Wang, Q.; Qiu, W.-Y.; *et al.* Mitigation of Metal-mediated Losses by Coating Au Nanoparticles with Dielectric Layer in Plasmonic Solar Cells. *RSC Adv.* **2013**, *3*, 16080–16088.
19. Standridge, S. D.; Schatz, G. C.; Hupp, J. T. Distance Dependence of Plasmon-Enhanced Photocurrent in Dye-Sensitized Solar Cells. *J. Am. Chem. Soc.* **2009**, *131*, 8407–8409.
20. Brown, M. D.; Suteewong, T.; Kumar, R. S. S.; D'Innocenzo, V.; Petrozza, A.; Lee, M. M.; Wiesner, U.; Snaith, H. J. Plasmonic Dye-sensitized Solar Cells Using Core-Shell Metal-Insulator Nanoparticles. *Nano Lett.* **2011**, *11*, 438–445.
21. Kawawaki, T.; Takahashi, Y.; Tatsuma, T. Enhancement of Dye-Sensitized Photocurrents by Gold Nanoparticles: Effects of Plasmon Coupling. *J. Phys. Chem. C* **2013**, *117*, 5901–5907.
22. Liu, W.-L.; Lin, F.-C; Yang, Y.-C.; Huang, C.-H.; Gwo, S.; Huang, M. H.; Huang, J.-S. The Influence of Shell Thickness of Au@TiO_2 Core-shell Nanoparticles on the Plasmonic Enhancement Effect in Dye-sensitized Solar Cells. *Nanoscale* **2013**, *5*, 7953–7962.
23. Zhang, W.; Saliba, M.; Stranks, S. D.; Sun, Y.; Shi, X.; Wiesner, U.; Snaith, H. J. Enhancement of Perovskite-Based Solar Cells Employing Core-Shell Metal Nanoparticles. *Nano Lett.* **2013**, *13*, 4505–4510.
24. Watanabe, R.; Miyano, K. Metal Nanoparticles in a Photovoltaic Cell: Effect of Metallic Loss. *AIP Adv.* **2011**, *1*, 042154.
25. Keuleyan, S.; Lhuillier, E.; Brajuskovic, V.; Guyot-Sionnest, P. Mid-infrared HgTe Colloidal Quantum Dot Photodetectors. *Nat. Photonics* **2011**, *5*, 489–493.
26. Chen, M.; Yu, H.; Kershaw, S. V.; Xu, H.; Gupta, S.; Hetsch, F.; Rogach, A. L.; Zhao, N. Fast, Air-Stable Infrared Photodetectors based on Spray-Deposited Aqueous HgTe Quantum Dots. *Adv. Funct. Mater.* **2014**, *24*, 53–59.

27. Pegg, L.-J.; Hatton, R. A. Nanoscale Geometric Electric Field Enhancement in Organic Photovoltaics. *ACS Nano* **2012**, *6*, 4722–4730.
28. Boyer, D.; Tamarat, P.; Maali, A.; Lounis, B.; Orrit, M. Photothermal Imaging of Nanometer-Sized Metal Particles Among Scatterers. *Science* **2002**, *297*, 1160–1162.
29. Govorov, A. O.; Richardson, H. H. Generating Heat with Metal Nanoparticles. *Nano Today* **2007**, *2*, 30–38.
30. Neumann, O.; Urban, A. S.; Day, J.; Lai, S.; Nordlander, P.; Halas, N. J. Solar Vapor Generation Enabled by Nanoparticles. *ACS Nano* **2013**, *7*, 42–49.
31. Rogach, A. L.; Kershaw, S. V.; Burt, M.; Harrison, M.; Kornowski, A.; Eychmüller, A.; Weller, H. Colloidally Prepared HgTe Nanocrystals with Strong Room-Temperature Infrared Luminescence. *Adv. Mater.* **1999**, *11*, 552–554.
32. Kovalenko, M. V.; Kaufmann, E.; Pachinger, D.; Roither, J.; Huber, M.; Stangl, J.; Hesser, G.; Schäffler, R.; Heiss, W. Colloidal HgTe Nanocrystals with Widely Tunable Narrow Band Gap Energies: From Telecommunications to Molecular Vibrations. *J. Am. Chem. Soc.* **2006**, *128*, 3516–3517.
33. Kershaw, S. V.; Susha, A. S.; Rogach, A. L. Narrow Bandgap Colloidal Metal Chalcogenide Quantum dots: Synthetic Methods, Heterostructures, Assembilies, Electronic and Infrared Optical Properties. *Chem. Soc. Rev.* **2013**, *42*, 3033–3087.
34. Shao, L.; Ruan, Q.; Jiang, R.; Wang, J. Macroscale Colloidal Noble Metal Nanocrystal Arrays and Their Refractive Index-Based Sensing Characteristics. *Small* **2013**, *10*, 802–811.
35. Suk, J. W.; Kitt, A.; Magnuson, C. W.; Hao, Y.; Ahmed, S.; An, J.; Swan, A. K.; Goldbery, B. B.; Ruoff, R. S. Transfer of CVD-Grown Monolayer Graphene onto Arbitrary Substrates. *ACS Nano* **2011**, *9*, 6916–6924.
36. Martins, L. G. P.; Song, Y.; Zeng, T.; Dresselhaus, M. S.; Kong, J.; Araujo, P. T. Direct Transfer of Grapheme onto Flexible Substrates. *Proc. Natl. Acad. Sci. U. S. A.* **2013**, 10.1073/pnas.1306508110.
37. Small, C. E.; Chen, S.; Subbiah, J.; Amb, C. M.; Tsang, S.-W.; Lai, T.-H.; Reynolds, J. R.; So, F. High-Efficiency Inverted Dithienogermole-thienopyrrolodione-based Polymer Solar Cells. *Nat. Photonics* **2012**, *6*, 115–120.
38. Rex, M.; Hernandez, F. E.; Campliglia, A. D. Pushing the Limits of Mercury Sensors with Gold Nanorods. *Anal. Chem.* **2006**, *78*, 445–451.
39. de Arquer, F. P. G; Beck, F. J.; Konstantatos, G. Absorption Enhancement in Solution Processed Metal-Semiconductor Nanocomposites. *Opt. Express* **2011**, *19*, 21038–21049.
40. Pai, D. M.; Enck, R. C. Onsager Mechanism of Photogeneration in Amorphous Selenium. *Phys. Rev. B: Solid State* **1975**, *11*, 5163–5174.
41. Braun, C. L. Electric Field Assisted Dissociation of Charge Transfer States as a Mechanism of Photocarrier Production. *J. Chem. Phys.* **1984**, *80*, 4157–4161.
42. Arkhipov, V. I.; Emelianova, E. V.; Bässler, H. Hot Exciton Dissociation in a Conjugated Polymer. *Phys. Rev. Lett.* **1999**, *82*, 1321–1324.
43. Tisdale, W. A.; Williams, K. J.; Timp, B. A.; Norris, D. J.; Aydil, E. S.; Zhu, X.-Y. Hot-Electron Transfer from Semiconductor Nanocrystals. *Science* **2010**, *328*, 1543–1546.
44. Grancini, G.; Maiuri, M.; Fazzi, D.; Petrozza, A.; Egelhaaf, H.-J.; Brida, D.; Cerullo, G.; Lanzani, G. Hot Exciton Dissociation in Polymer Solar Cells. *Nat. Mater.* **2012**, *12*, 29–33.
45. Strein, E.; deQuilettes, D. W.; Hsieh, S. T.; Colbert, A. E.; Ginger, D. S. Hot Hole Transfer Increasing Polaron Yields in Hybird Conjugated Polymer/PbS Blends. *J. Phys. Chem. Lett.* **2014**, *5*, 208–211.
46. Al-Otaify, A.; Kershaw, S. V.; Gupta, S.; Rogach, A. L.; Allan, G.; Delerue, C.; Binks, D. J. Multiple Exciton Generation and Ultrafast Exciton Dynamics in HgTe Colloidal Quantum Dots. *Phys. Chem. Chem. Phys.* **2013**, *15*, 16864–16873.
47. Dereniak, E. L.; Boreman, G. D. *Infrared Detectors and Systems*; John Wiley and Sons, Inc.: New York, 1996; Chapter 5, Vol. 6, p 8.
48. Rinnerbauer, V.; Hingerl, K.; Kovalenko, M.; Heiss, W. Effect of Quantum Confinement on Higher Transitions in HgTe Nanocrystals. *Appl. Phys. Lett.* **2006**, *89*, 193114.